

# In Situ Transformation of MOFs into Layered Double Hydroxide Embedded Metal Sulfides for Improved Electrocatalytic and Supercapacitive Performance

Gamze Yilmaz, Kah Meng Yam, Chun Zhang, Hong Jin Fan, and Ghim Wei Ho\*

Direct adoption of metal-organic frameworks (MOFs) as electrode materials shows impoverished electrochemical performance owing to low electrical conductivity and poor chemical stability. In this study, we demonstrate self-templated pseudomorphic transformation of MOF into surface chemistry rich hollow framework that delivers highly reactive, durable, and universal electrochemically active energy conversion and storage functionalities. In situ pseudomorphic transformation of MOF-derived hollow rhombic dodecahedron template and sulfurization of nickel cobalt layered double hydroxides (NiCo-LDHs) lead to the construction of interlayered metal sulfides (NiCo-LDH/Co<sub>9</sub>S<sub>8</sub>) system. The embedment of metal sulfide species (Co<sub>9</sub>S<sub>8</sub>) at the LDH intergalleries offers optimal interfacing of the hybrid constituent elements and materials stability. The hybrid NiCo-LDH/Co<sub>9</sub>S<sub>8</sub> system collectively presents an ideal porous structure, rich redox chemistry, and high electrical conductivity matrix. This leads to a significant enhancement in its complementary electrocatalytic hydrogen evolution and supercapacitive energy storage properties. This work establishes the potential of MOF derived scaffold for designing of novel class hybrid inorganic–organic functional materials for electrochemical applications and beyond.

structural merits of low mass density, large surface area, surface permeability, high loading capacity, and shortened diffusion paths for enhanced mass and charge transport.<sup>[1]</sup> These properties render them promising candidates in diverse energy conversion and storage applications. Over the past decades, templating approach has proven its efficacy in synthesizing well-defined hollow structures.<sup>[2]</sup> However, intricate synthesis steps, such as surface modification and core template removal (needing toxic etchants) often result in low reproducibility, high cost, and poor uniformity hollow nanostructures. Moreover, it is challenging to introduce functional chemical species into the hollow and porous intercrystalline structure with exceptional homogeneity and dispersity. Instead, agglomeration and loading of the chemical species on outer surfaces often occur which lead to nonoptimal chemical interaction and pore blockage issues. All these obstacles limit the realization of

Developments in alternative clean fuel and energy storage technologies come forth as strong contenders to fossil-based sources. As such, electrochemically active hollow nanostructured materials are judiciously investigated due to their unique

well-coordinated heterospecies hollow structures with advanced functional properties.

As a novel subclass of porous metal-organic frameworks (MOFs), zeolitic imidazole frameworks (ZIFs) comprise of coordinated inorganic clusters and organic linkers, and have been recognized to be dual-functioning materials serving as both sacrificial templates and metal precursors toward construction of well-defined hollow structures.<sup>[3]</sup> Specifically, self-templated ZIFs engage assembly of metal ions and polydentate organic ligands at precursor level which favorably eliminate the template removal processing steps and ease the fabrication of multi-metal hollow structures with molecular controllable composition. Recently, multi-metallic MOFs that deploy two metals have been designed to augment electrical conductivity as opposed to mono-metallic system.<sup>[4]</sup> Distinctively, the layered hydroxides promote intercalation of ions at the interlayers that decreases mass transport resistance while the sulfides improve the electrical conductivity owing to reduced bandgap.<sup>[5]</sup> Besides, heteroatomic species explicitly metal hydroxides and sulfides have shown to offer overwhelming richness in electrochemically active properties as compare to the oxide counterpart. Despite the remarkable progresses made in the synthesis of hollow nanostructures, heteroatomic MOF-derived system with incorporated functional chemical species layered double hydroxide (LDH) nanosheets remains largely unexplored thus far.

G. Yilmaz, Prof. G. W. Ho  
Department of Electrical and Computer Engineering  
National University of Singapore  
4 Engineering Drive 3, Singapore 117583, Singapore  
E-mail: elehgw@nus.edu.sg

G. Yilmaz  
Department of Chemical and Biomolecular Engineering  
National University of Singapore  
4 Engineering Drive 4, Singapore 117583, Singapore

K. M. Yam, Prof. C. Zhang  
Department of Physics and Chemistry  
National University of Singapore  
2 Science Drive 3, Singapore 117583, Singapore

Prof. H. J. Fan  
School of Physical and Mathematical Sciences  
Nanyang Technological University  
Singapore 117583, Singapore

Prof. G. W. Ho  
Engineering Science Programme  
National University of Singapore  
9 Engineering Drive 1, Singapore 117583, Singapore

DOI: 10.1002/adma.201606814

Given the adaptability of self-templated MOFs in construction of multi-metallic hollow structures and apparent merits of heteroatomic hydroxides and sulfides moieties, we devise the synthesis of MOF-derived LDH entrapped interlayered metal sulfides system that possesses synergetic electrochemical properties within an integral framework. Sacrificial ZIF template is exploited to accomplish in situ homogenous pseudomorphic chemical transformation of nickel cobalt layered double hydroxides (NiCo-LDHs) into hybrid NiCo-LDH/cobalt sulfide ( $\text{Co}_9\text{S}_8$ ) system. The  $\text{Co}_9\text{S}_8$  species are purposefully incorporated within the spatially confined interlayered structure to considerably enhance the stability and reactivity of the material. The hybrid multi-metallic-heteroatomic MOF derivative exhibits superior electrochemical performance and remarkable stability as supercapacitor and electrocatalyst electrode material. The complementary electrochemical measurements and density functional theory computations show that the combination of multi-metallic-heteroatomic constitution and hollow structure significantly enhances the electrical conductivity and the free energy for  $\text{H}_2\text{O}$  adsorption.

The schematic in **Figure 1a** demonstrates the strategy for the synthesis approach of NiCo-LDH/ $\text{Co}_9\text{S}_8$  hybrid, and its distinctive difference from the prior works is illustrated in Figure S1a in the Supporting Information. A room temperature precipitation process is employed to synthesize well-defined, monodispersed ZIF-67 crystals using cobalt ions as the metallic node and 2-methyl imidazole as the organic linker in methanol solution. As-prepared ZIF-67 evolves into uniform rhombic dodecahedron shape with 12 congruent rhombic faces and 24 edges with an average particle size of 700 nm (Figure S1b, Supporting Information). To probe the chemical identity, the crystals were characterized by X-ray diffraction (XRD) (Figure S2, Supporting Information). All diffraction peaks can be readily indexed to ZIF-67 and match well with the reported and simulated works.<sup>[3c,d]</sup> As-synthesized ZIF-67 crystals were then thermally

treated under nitrogen ( $\text{N}_2$ ) at 400 °C for 2h to remove physically attached groups and enhance the amorphous carbon content of the final product. The scanning electron microscopy (SEM) and transmission electron microscopy (TEM) images (Figure 1b,e) show that annealed ZIF-67 (ZIF-67-C) retains the overall morphology of the framework with an apparent inner wall contraction toward the center (Figures S3–S5, Supporting Information). This structural shrinkage can be attributed to the cross-linking of the organic ligands which is corroborated by the thermogravimetric analysis (TGA) analysis showing the decomposition onset of ZIF-67 around 400 °C (Figure S6, Supporting Information).<sup>[3d]</sup> Subsequently, the LDH was synthesized through the release of hydroxyl and nickel ions from the hydrolysis of nickel nitrate in ethanol, possible partial oxidation of  $\text{Co}^{2+}$  ions by  $(\text{NO}_3)^-$  ions and dissolved oxygen in the solution, subsequent coprecipitation of  $\text{Co}^{2+}/\text{Co}^{3+}$  with  $\text{Ni}^{2+}$ , and gradual etching of ZIF-67 template by the protons released from the hydrolysis process of nickel ions.<sup>[6]</sup> The ZIF-67-C derived NiCo-LDH (C/LDH) maintains the rhombic dodecahedral structure (Figure 1c,f). Subsequently, the C/LDH was sulfurized to yield the NiCo-LDH/ $\text{Co}_9\text{S}_8$  hybrid (C/LDH/S) (Figure 1d,g). The extent of sulfurization was optimized without compromising the structural integrity and LDH characteristic features (Figure S7, Supporting Information). Figure 1d and inset show the typical SEM images of the C/LDH/S which exhibit the polyhedron morphology, hence retaining the original sacrificial template structure.

The crystallinity and cooccurrence of the phases in C/LDH/S were investigated by XRD. NiCo-LDH (denoted as LDH) was also prepared using as-synthesized ZIF-67, which is not thermally treated under  $\text{N}_2$  at 400 °C (Figures S8 and Figure S9, Supporting Information). All diffraction patterns of LDH (**Figure 2a**) are indexed to (003), (006), (009), and (110) plane reflections of the hydrotalcite-like LDH phase with corresponding  $2\theta$  values of 10.9°, 22.1°, 33.5°, and 60.3°.<sup>[7]</sup> All

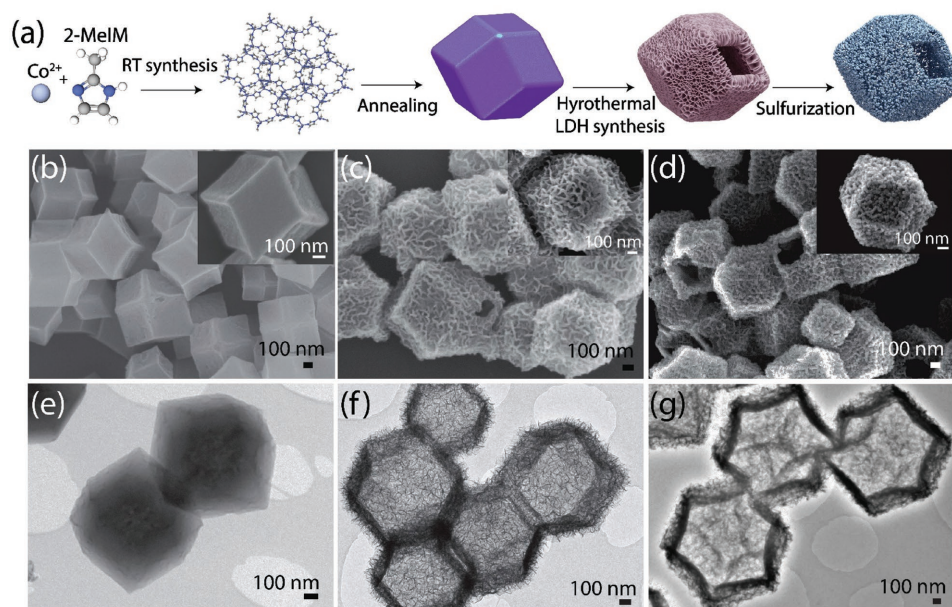


**Figure 1.** a) Schematic illustration for the synthesis process of hollow NiCo-LDH/ $\text{Co}_9\text{S}_8$  hybrid. Panoramic and single (inset) SEM images of b) ZIF-67-C, c) C/LDH, and d) C/LDH/S polyhedrons. TEM images of e) ZIF-67-C, f) C/LDH, and g) C/LDH/S polyhedrons.

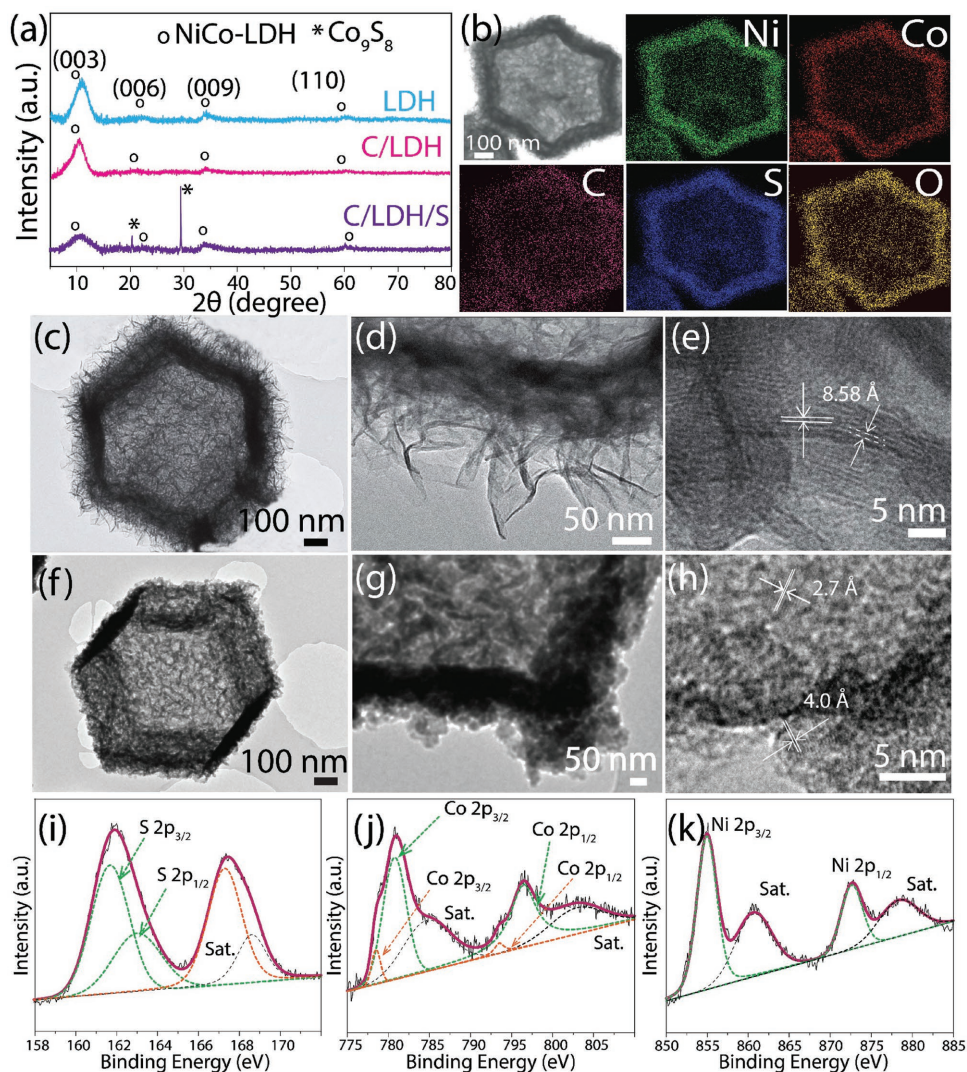


**Figure 2.** a) The representative XRD patterns for as-prepared LDH, C/LDH, and C/LDH/S. b) Elemental mapping of C/LDH/S for Ni, Co, C, O, and S. TEM and high-resolution TEM images of c–e) C/LDH and f–h) C/LDH/S. High-resolution i) S 2p, j) Co 2p, and k) Ni 2p XPS spectra for C/LDH/S.

ZIF-67 diffraction peaks are absent indicating the complete conversion to LDH phase. Similar to LDH, C/LDH exhibits distinguished peaks corresponding to the (00*n*) planes demonstrating successful preparation of LDH phase from the ZIF-67-C. According to the XRD peak positions, the interlayer spacing increased from 8.10 to 8.58 Å after calcination treatment. The change in interlayer spacing may be attributed to the modification of interlayer occupying anion, which compensates the positive charge of brucite-like layers, after the thermal process. This is due to the cross-linking of the organic ligand with removal of –OH groups and solvent/water/moisture inside the ZIF material, which may further affect the formation of anionic compound.<sup>[8]</sup> Moreover, the formation of amorphous carbon after 400 °C calcination treatment was confirmed by Raman spectrum of C/LDH (Figure S10, Supporting Information), representing two characteristic peaks at 1335 and 1580 cm<sup>-1</sup>. After sulfurization, C/LDH/S displays the LDH plane reflections with the emergence of new peaks as an indication of a new crystal phase formation. The two obvious diffraction peaks

appearing in the XRD pattern (Figure 2a) match well with the characteristics (200) and (311) reflections of cubic Co<sub>9</sub>S<sub>8</sub> phase (JCPDS card no 19-0364).<sup>[9]</sup>

The structural features and chemical composition of C/LDH and C/LDH/S were further characterized using TEM. The outer frame of the C/LDH structure is densely decorated by interconnected nanosheets covering the well-defined hollow interior (Figure 2c). The hollow structure of C/LDH demonstrates the successful etching process. Similarly, by adjusting the reaction conditions, ZIF-67 core/NiCo-LDH shell structures can also be synthesized (Figure S11, Supporting Information). After sulfurization, the uniformly distributed nanosheets on the shell of the C/LDH become thicker (Figure 2f). High-resolution TEM images recorded from the edge regions of the C/LDH (Figure 2d,e) reveals a lattice spacing of 8.58 Å, which is in good agreement with the (003) plane of ZIF-67-C derived NiCo-LDH. In the case of C/LDH/S (Figure 2g,h), two lattice fringes with different spacing are detected, namely 4.0 and 2.7 Å, corresponding to the (006) and (311) planes of NiCo-LDH and

Co<sub>9</sub>S<sub>8</sub>, respectively. This indicates the hybrid nature of the C/LDH/S. Furthermore, the uniform distribution of Ni, Co, O, S, and C across the structure was mapped using energy dispersive X-ray spectroscopy (EDX) as presented in Figure 2b.

X-ray photoemission spectroscopy (XPS) was also performed to provide insight on the chemical states of elements in C/LDH/S. The XPS data survey spectrum of C/LDH/S (Figure S12, Supporting Information) shows the existence of Ni, Co, S, O, and C elements, which is in agreement with the EDX analysis. The atomic percentage of the elements for each sample is shown in Table S1, which suggests the formation of Ni<sub>0.7</sub>Co<sub>0.3</sub>-LDH complex (Ni:Co ≈ 2.5) for both LDH and C/LDH before sulfur treatment. The electronic state of sulfur in C/LDH/S is carefully investigated, the S 2p peaks at 161.7 and 163.0 eV is attributed to the S 2p<sub>3/2</sub> and S 2p<sub>1/2</sub> orbitals of Co<sub>9</sub>S<sub>8</sub> (Figure 2i).<sup>[10]</sup> The combination of LDH characteristic features and the sulfide compound corroborates the hybrid nature of C/LDH/S. Besides, S 2p spectra of C/LDH/S displays one additional peak at 167.3 eV, corresponding to oxidized sulfur groups (–C–SO<sub>x</sub>–C–, *x* = 2–4), such as sulfate or sulfonate, in agreement with the C–S peak (Figure S13c, Supporting Information) observed at 283.8 eV.<sup>[11]</sup> This is also consistent with the Fourier transform infrared spectroscopy (FTIR) spectrum of C/LDH/S (Figure S14, Supporting Information). Meanwhile, the core level spectrum of Co 2p (Figure 2j) can be divided into two spin-orbit doublets. The doublet at 781.0 (Co 2p<sub>3/2</sub>) and 796.4 eV (Co 2p<sub>1/2</sub>) shows the Co 2p characteristics of NiCo-LDH, while the doublet at 778.4 (Co 2p<sub>3/2</sub>) and 793.5 eV (Co 2p<sub>3/2</sub>) is in accordance with the formation of Co<sub>9</sub>S<sub>8</sub>.<sup>[7b,10,12]</sup> For Ni 2p spectra (Figure 2k), a significant spin-orbit doublet, with two shake-up satellites, are located at 872.8 and 855.2 eV, which can be ascribed to the Ni 2p<sub>3/2</sub> and Ni 2p<sub>1/2</sub> signals of Ni<sup>2+</sup>, respectively.<sup>[7,13]</sup>

The FTIR analysis (Figure S14, Supporting Information) and TGA (Figure S15, Supporting Information) investigations were further performed to gain information about the intercalation nature of the layered double hydroxides. The NO<sub>3</sub><sup>–</sup> ions are found to be the interlayer anions between the brucite-like layers in LDH and C/LDH and its existence is supported by N 1s XPS spectra (Figure S16, Supporting Information). This is also consistent with the XRD analysis depicting LDH interlayer spacing of 8.10 Å, which is in the range of the hydrocalcite-like compounds with NO<sub>3</sub><sup>–</sup> interlayer anions.<sup>[14]</sup> Moreover, smaller sized CO<sub>3</sub><sup>2–</sup> ion is also known of its strong affinity to cationic host LDH layers and its identity was confirmed by the C 1s XPS spectra (Figure S13a, Supporting Information).<sup>[8b,14b,15]</sup> In case of C/LDH, the C 1s spectra can be divided into several peaks corresponding to C–C (284.5 eV), C–O

(285.1 eV), and C–N (287.2 eV), showing the intercalation of different carbon-based functional groups between the layers (Figure S13b, Supporting Information).<sup>[11b–d]</sup> We further carried out TGA (Figure S15, Supporting Information) to understand the anions in the gallery region of the LDH since thermal decomposition behavior of the LDH is strongly related to the nature of the intercalated counteranions.<sup>[16]</sup> Although C/LDH and LDH have similar characteristic thermal behavior, temperature intervals required for decomposition and the amount of water removed from the structure is different. The decomposition/collapse onset temperature of the C/LDH (289 °C) is found to be higher than that of the LDH (245 °C), showing its higher thermal stability. Moreover, C/LDH (11.1 wt%) has higher water/hydroxyl content compared with LDH (7.8 wt%), which further supports the broader interspace distance as observed in XRD pattern (Figure 2a) and consistent with the occupation of larger interlayer carbon-based anion between the double hydroxide layers besides the nitrate anions. As for C/LDH/S, the thermal behavior indicates the presence of sulfur

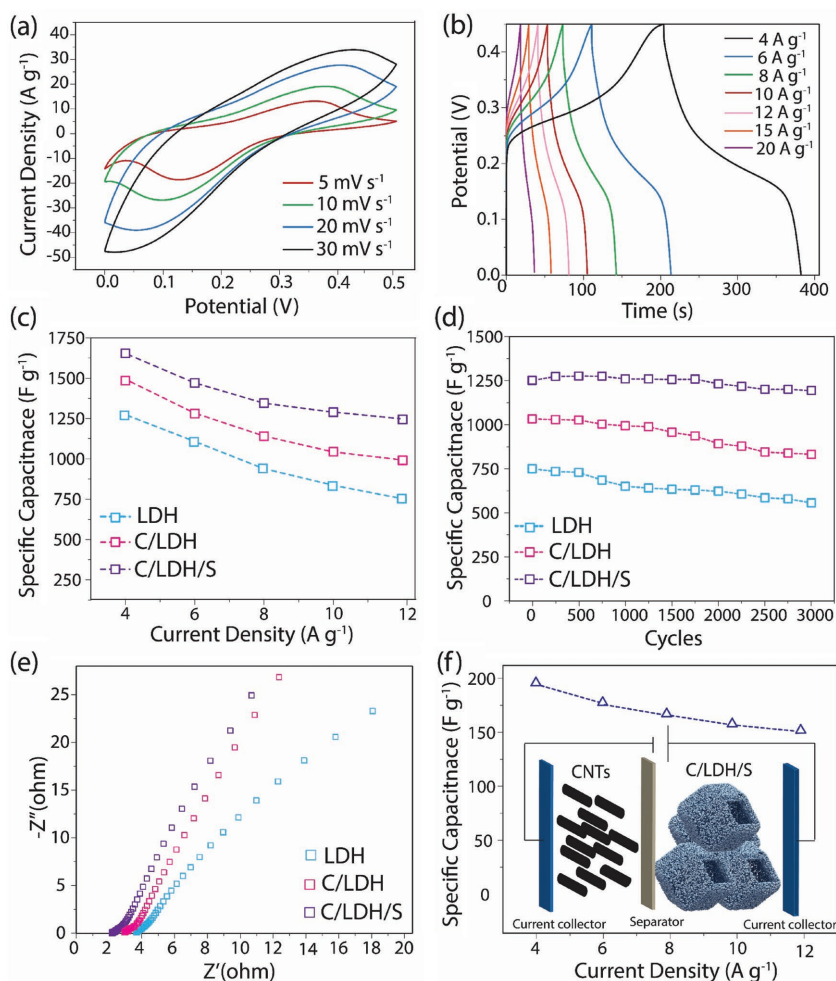


**Figure 3.** Supercapacitive performance. a) CV curves at various scan rates; b) charge–discharge profiles at various current densities for C/LDH/S. c) Specific capacitances as a function of current density, d) cycling stability tests over 3000 cycles, and e) Nyquist plots in a frequency range from 0.01 Hz to 100 kHz for the electrodes. f) Calculated specific capacitance values for C/LDH/S//CNTs asymmetric supercapacitor cell. Inset is the schematic illustration of the cell.

containing functionalities. Although the determination of the precise nature of the interlayer region is difficult, we propose the presence of different intergallery anions in LDH, C/LDH, and C/LDH/S structures, since the intercalation reactions are generally nonselective processes and can be affected by the reaction conditions.<sup>[17]</sup>

High surface area brings exceptional electrochemical properties owing to rich electrode/electrolyte interfacial area for electrochemical reactions. Together with hollow architecture, it combines the advantages of easily accessible active surface sites and rapid transportation of electrolyte, resulting in an improved electrochemical performance. Hence, surface area and porosity properties of C/LDH/S were studied by N<sub>2</sub> adsorption/desorption measurements and presented in Figure S17 in the Supporting Information and Table S2 in the Supporting Information. A specific surface area of 116.2 cm<sup>2</sup> g<sup>-1</sup> with a pore volume of 0.439 cm<sup>3</sup> g<sup>-1</sup> was obtained using the multipoint Brunauer–Emmett–Teller method. As such, capacitive performances of supercapacitor electrodes based on C/LDH/S were investigated using a three-electrode system in 1 M KOH aqueous electrolyte. **Figure 3a** shows the representative cyclic voltammetry (CV) curves of the C/LDH/S at various scan rates in the potential range of 0–0.5 V (vs saturated calomel electrode (SCE)). Greater accessibility of electrolyte ions through the electrode surface at low sweep rates has resulted in distinguishable symmetric anodic and cathodic peaks at 5 mV s<sup>-1</sup>, suggesting the pseudo-capacitive characteristics of the electrode (Figure S18, Supporting Information). This arises from reversible faradaic reactions associated with the nickel and cobalt hydroxide/sulfide.<sup>[13,18]</sup> At higher scan rates, anodic and cathodic peaks are shifted to more negative and positive potentials, respectively, owing to the increase in the internal resistance of the electrode.

The galvanostatic charge–discharge (CD) profiles were also measured at different current densities (4 to 20 A g<sup>-1</sup>) and presented in Figure 3b. The symmetric CD profiles are an indication of good capacitive behavior with highly reversible and fast reaction kinetics. Based on the CD curves, the specific capacitance ( $C_{sp}$ ) was calculated at different current densities using the following equation

$$C_{sp} = i\Delta t/m\Delta V \quad (1)$$

where  $i$  (in A) is the discharge current,  $\Delta t$  (in s) is the discharge time,  $m$  (in g) is the mass of active material, and  $\Delta V$  (in V) is the potential drop in discharge (excluding the ohmic potential drop). The specific capacitances obtained for C/LDH/S are 1653, 1470, 1345, 1288, 1249, 1145, and 1025 F g<sup>-1</sup> at current densities of 4, 6, 8, 10, 12, 15, and 20 A g<sup>-1</sup>

(Figure 3c), respectively. The C/LDH/S electrode shows relatively high specific capacitance and excellent cycling stability (95.4% after 3000 cycles) (Figure 3d) as compared to prior works (Table S3, Supporting Information). To understand the synergistic effect originating from the coexistence of NiCo-layered double hydroxide and cobalt sulfide, and the effect of calcination step, electrochemical performance of sulfurized layered double hydroxide (LDH/S) (Figure S19, Supporting Information), as well as LDH and C/LDH, was evaluated. LDH, C/LDH, LDH/S, and C/LDH/S deliver specific capacitances of 1275, 1493, 1511, and 1653 F g<sup>-1</sup> at 4 A g<sup>-1</sup>, respectively. Comparatively, C/LDH/S shows 22.0%, 12.0%, and 14.9% higher rate capabilities than LDH, C/LDH, and LDH/S, respectively. Moreover, effect of Co<sub>9</sub>S<sub>8</sub> loading on supercapacitor performance of C/LDH/S was investigated for C/LDH/S hybrids containing ≈10 (C/LDH/S-10), ≈20 (C/LDH/S), and ≈30 wt% (C/LDH/S-30) cobalt sulfide (Figures S20 and S21, Supporting

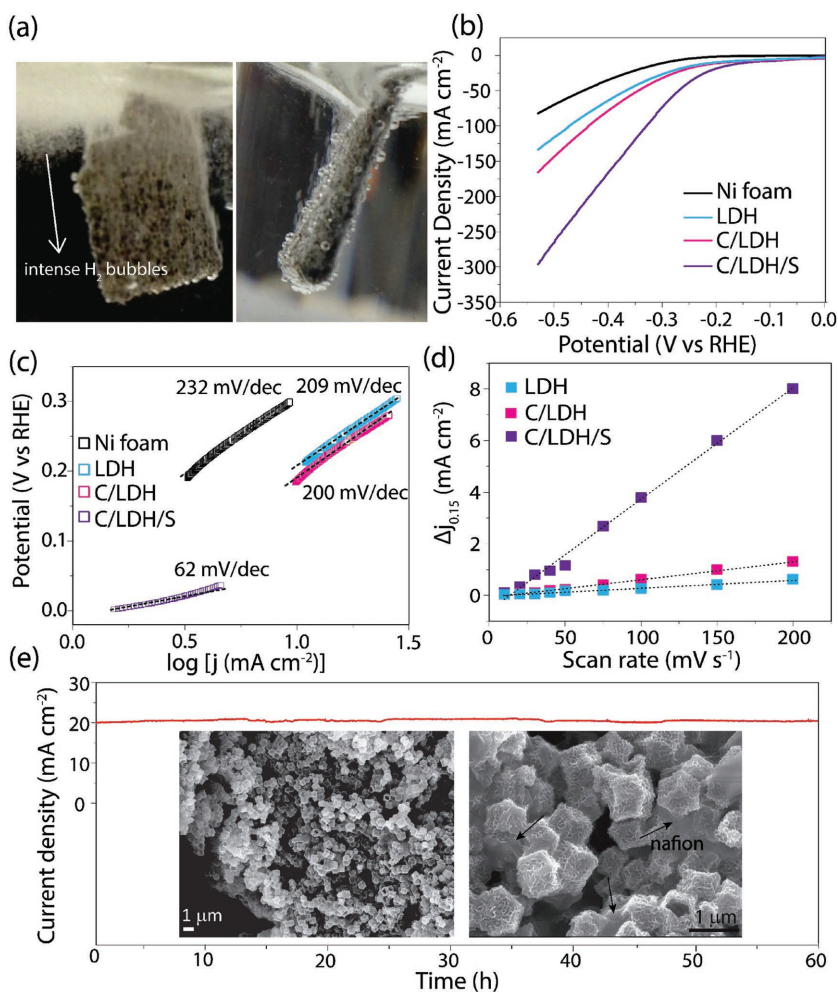


**Figure 4.** Electrochemical performance. a) Digital images for the evolution of H<sub>2</sub> bubbles, captured at 0.35 V during LSV test of C/LDH/S. b) HER polarization curves for nickel foam (Ni foam), LDH, C/LDH, and C/LDH/S at a scan rate of 5 mV s<sup>-1</sup> and c) corresponding Tafel plots for the electrocatalysts. d) Current density differences calculated at 0.15 V from the cyclic voltammetry curves collected at various scan rates in the region where no redox peaks are observed (0.1–0.2 V). e) Time-dependent current curve for C/LDH/S under static overpotential for 60 h. Inset shows the different magnification SEM images for C/LDH/S after 60 h stability test.

Information). C/LDH/S with  $\approx 20\%$  weight percentage of  $\text{Co}_9\text{S}_8$  in the C/LDH/S hybrid exhibits the optimum performance among the samples investigated.

We further investigated the transport characteristics of the LDH, C/LDH, and C/LDH/S by electrochemical impedance spectroscopy to understand their electrochemical behavior. Equivalent series resistance of C/LDH/S is found to be  $2.21 \Omega$ , smaller than that for C/LDH ( $2.88 \Omega$ ) and LDH ( $3.53 \Omega$ ) as presented in Figure 3e. Smaller charge transfer resistance of C/LDH/S, determined from the diameter of the semicircle, and improved ion diffusion, suggested by the higher angle vertical line, substantiate the enhanced electrochemical properties of C/LDH/S. Furthermore, LDH derived from calcined ZIF-67 (C/LDH) resulted in augmented supercapacitive properties compared to the pristine LDH. This improvement can be attributed to enlarged interlayer spacing of C/LDH and increased amorphous carbon content, which facilitate electrolyte penetration for fast diffusion and reaction, leading to higher reaction kinetics.<sup>[16c]</sup>

An asymmetric supercapacitor device with two-electrode configuration (see the details in Figure S22, Supporting Information) was assembled using C/LDH/S and carbon nanotubes (CNTs) as positive and negative electrodes, respectively. A specific capacitance of  $194 \text{ F g}^{-1}$  is calculated at  $4 \text{ A g}^{-1}$  (Figure S22c, Supporting Information), which decreases to  $151 \text{ F g}^{-1}$  at  $12 \text{ A g}^{-1}$ , showing a superior rate capability of  $77.8\%$  (Figure 3f). Furthermore, C/LDH/S//CNTs exhibits a high stability with  $90.9\%$  retention of the initial capacitance (Figure S22e, Supporting Information) when cycled for 10 000 cycles at  $8 \text{ A g}^{-1}$ . The cell also delivers a high energy density of  $39 \text{ Wh kg}^{-1}$  at the lowest power density of  $2.4 \text{ kW kg}^{-1}$  when the current density is  $4 \text{ A g}^{-1}$ , and it can hold  $30.1 \text{ Wh kg}^{-1}$  even at the highest power density of  $7.4 \text{ kW kg}^{-1}$  (Figure S22f, Supporting Information).

To date, transition metal chalcogenides have shown to be highly active hydrogen evolution reaction (HER) electrocatalysts under acidic conditions. Specifically, great efforts have been devoted to dichalcogenides since their active sites resemble to that of nitrogenase/hydrogenase. However, considering the vulnerability of most HER catalysts in acidic solutions and the commercialization of hydrogen production from alkaline electrolyzer, it is highly desirable to develop HER catalyst with high activity and stability operable at basic pH.<sup>[19]</sup> Recently, cobalt sulfides have been demonstrated as active catalysts in alkaline medium and their activities was shown to be enhanced by incorporation of a secondary transition metal due to decrease in the adsorption energy of hydrogen in the first step of HER reaction pathway :



where  $M$  stands for metal atom and  $\text{H}_{\text{ads}}$  indicates adsorbed hydrogen atom on active site.<sup>[20]</sup> On this basis, we further evaluated

the as-synthesized hollow MOF-derived materials as electrocatalysts for HER in  $1.0 \text{ M KOH}$  solution. The HER electrocatalytic activities of pure nickel foam, LDH, C/LDH, C/LDH/S, and  $\text{Co}_9\text{S}_8/\text{C}$  were first tested by linear sweep voltammetry (LSV) from 0 to  $-0.6 \text{ V}$  (vs reversible hydrogen electrode (RHE)) with a typical three-electrode set up. Intense vigorous  $\text{H}_2$  bubbles were observed during the measurements of C/LDH/S electrode showing its high electrocatalytic activity (Figure 4a). The representative polarization curves of the electrocatalysts are shown in Figure 4b and Figure S23 in the Supporting Information. Compared to pure nickel foam, LDH, C/LDH, and  $\text{Co}_9\text{S}_8/\text{C}$ , C/LDH/S requires a lower onset potential of  $47 \text{ mV}$  and an overpotential of  $142 \text{ mV}$  to drive the cathodic current density of  $10 \text{ mA cm}^{-2}$ . In contrast, higher overpotentials of  $294$ ,  $201$ ,  $185$ , and  $155 \text{ mV}$  are required to drive the same current density for bare nickel foam, LDH, C/LDH, and  $\text{Co}_9\text{S}_8/\text{C}$ , respectively. The HER kinetics of the catalysts was further studied through the Tafel plots (Figure 4c, Figure S23d, Supporting Information). C/LDH/S exhibits the smallest slope of  $62 \text{ mV dec}^{-1}$ , exhibiting the highest electrocatalytic activity and kinetics toward HER among all other samples in alkaline electrolyte. The electrocatalytic performance is comparable to other reported electrocatalysts (Table S4, Supporting Information). Moreover, investigations for the effect of  $\text{Co}_9\text{S}_8$  loading on HER performance of C/LDH/S indicated an optimum cobalt sulfide loading of  $\approx 20 \text{ wt}\%$  (Figure S24, Supporting Information).

As the catalytic activity is affected by the amount of active sites, the electrochemically active surface area of the electrocatalysts are compared by measuring the double layer capacitance ( $C_{\text{dl}}$ ) in non-Faradic region at different scan rates (Figure 4d).<sup>[21]</sup> C/LDH/S possesses significantly higher  $C_{\text{dl}}$  than that of the C/LDH and LDH, in agreement with its markedly higher HER

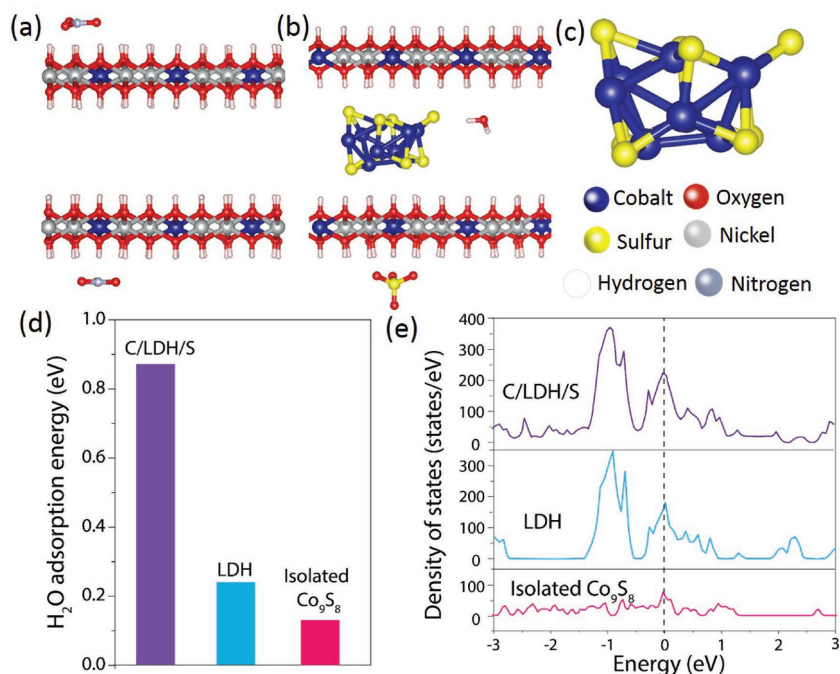


**Figure 5.** Optimized atomic configurations of a) C/LDH, b) NiCo-LDH/ $\text{Co}_9\text{S}_8$  (C/LDH/S), and c) isolated  $\text{Co}_9\text{S}_8$ . d) Calculated  $\text{H}_2\text{O}$  adsorption energies and e) density of states for C/LDH, NiCo-LDH/ $\text{Co}_9\text{S}_8$  (C/LDH/S) and isolated  $\text{Co}_9\text{S}_8$  catalysts. The Fermi level is set at 0 eV.

activity. Correspondingly, the electrochemical impedance measurements of C/LDH/S exhibits lower impedance and thus considerably accelerate HER kinetics (Figure S25, Supporting Information). Considering the importance of the durability of the electrocatalysts, chronoamperometric measurement with a static potential corresponding to  $20 \text{ mA cm}^{-2}$  was carried out over 60 h and presented in Figure 4e. It is noteworthy that no apparent HER activity degradation is recorded, implying the excellent durability of the C/LDH/S electrocatalyst. Such high stability is believed to correlate with well retention of the initial morphology of C/LDH/S after 60 h stability test (Figure 4e inset).

To provide further insight on the excellent HER electrocatalytic activity of multi-metallic NiCo-LDH/Co<sub>9</sub>S<sub>8</sub> (C/LDH/S) hybrid and shed light on the synergistic effects between C/LDH and Co<sub>9</sub>S<sub>8</sub>, density functional theory calculations were carried out. The optimized atomic configurations of C/LDH interlayered with nitrate ions, NiCo-LDH/Co<sub>9</sub>S<sub>8</sub> hybrid and isolated Co<sub>9</sub>S<sub>8</sub> are presented in Figure 5a–c, respectively. In view of the importance of water adsorption on catalysis as the first step, the chemisorption of the H<sub>2</sub>O on the optimized structures was studied (Figure S26, Supporting Information) and shown in Figure 5d. The NiCo-LDH/Co<sub>9</sub>S<sub>8</sub> hybrid exhibits H<sub>2</sub>O chemisorption energy (absolute) of 0.87 eV, which is much higher than C/LDH (0.24 eV) and Co<sub>9</sub>S<sub>8</sub> (0.14 eV), signifying enhanced water adsorption attributes of the hybrid system. Meanwhile, the electronic properties of the species were investigated by the density of states analysis (Figure 5e). The C/LDH possesses high density of states across the Fermi level without any gap, suggesting a high conductive behavior, whereas the isolated Co<sub>9</sub>S<sub>8</sub> exhibits continuous and gapless states, however of a less intense nature. The NiCo-LDH/Co<sub>9</sub>S<sub>8</sub> hybrid combines the unique advantages of individual C/LDH and Co<sub>9</sub>S<sub>8</sub> catalysts, which is observable from the increased and continuous electronic states. The synergistic effect between the layered double hydroxide and cobalt sulfide results in high electrical conductivity and metallic-like charge transfer, and through the van der Waals and hydrogen bond interactions, significant water adsorption is realized. The synergistic effect between the layered double hydroxide and cobalt sulfide has been realized through high electrical conductivity arising from the collaborative contribution of C/LDH and Co<sub>9</sub>S<sub>8</sub> to the metallic-like charge transfer. Combination of continuous density of states of cobalt sulfide together with the intense density of states of the layered double hydroxide, C/LDH/S system ensure abundant and extended electron active sites, substantial charge carrier concentration, and thus it offers enhanced electron mobility throughout the structure. Therefore, introduction of cobalt sulfide into the layered double hydroxide structure has proved to be an effective strategy to modify the electronic properties and paved the way for a more electrochemically active sulfide/hydroxide hybrid. Importantly, through the van der Waals and hydrogen bond interactions, which ensure the coexistence of sulfide/hydroxide hybrid, the most favorable H<sub>2</sub>O adsorption was obtained on C/LDH/S system, whereas less favorable H<sub>2</sub>O adsorption activities were observed on individual C/LDH and Co<sub>9</sub>S<sub>8</sub>. Thus, above results further confirm that hybrid C/LDH/S can achieve excellent HER catalytic attributes compared with layered double hydroxide and cobalt sulfide, suggesting their synergistic effect.

In summary, a self-templated MOF pseudomorphic transformation strategy to synthesize hollow multi-metallic-heteroatomic polyhedra has been established for the first time. Based on pseudomorphic substitution through ZIF-derived template, hybrid NiCo-LDH/Co<sub>9</sub>S<sub>8</sub> hollow system is constructed. The homogeneous incorporation of multiple metallic species, the creation of heterosulfides-hydroxides and the disposition of hollow structure optimize the catalytic sites, electrical conductivity, and hydrogen adsorption of the NiCo-LDH/Co<sub>9</sub>S<sub>8</sub>. When employed as supercapacitor and electrocatalyst electrode, the NiCo-LDH/Co<sub>9</sub>S<sub>8</sub> demonstrates significantly improved electrochemical performances and outstanding stability. This MOF-templated preparation scheme can possibly be extended to the preparation of other porous constituents MOFs composites, which may be exploited for diverse potential applications in energy storage, conversion, or environmental purposes.

## Supporting Information

Supporting Information is available from the Wiley Online Library or from the author.

## Acknowledgements

This work was supported by MOE R-263-000-B38-112 and R-263-000-B63-112 (Ministry of Education, Republic of Singapore).

## Conflict of Interest

The authors declare no conflict of interest.

## Keywords

electrocatalysts, hydrogen evolution reaction, layered double hydroxides, metal organic frameworks, supercapacitors

Received: December 16, 2016

Revised: March 29, 2017

Published online: May 3, 2017

- [1] X. Lai, J. E. Halpert, D. Wang, *Energy Environ. Sci.* **2012**, *5*, 5604.
- [2] X. Wang, J. Feng, Y. Bai, Q. Zhang, Y. Yin, *Chem. Rev.* **2016**, *116*, 10983.
- [3] a) L. Wang, Y. Han, X. Feng, J. Zhou, P. Qi, B. Wang, *Coord. Chem. Rev.* **2016**, *307*, 361; b) L. Hu, Q. Chen, *Nanoscale* **2014**, *6*, 1236; c) Y. Z. Zhang, Y. Wang, Y. L. Xie, T. Cheng, W. Y. Lai, H. Pang, W. Huang, *Nanoscale* **2014**, *6*, 14354; d) J. Shao, Z. Wan, H. Liu, H. Zheng, T. Gao, M. Shen, Q. Qu, H. Zheng, *J. Mater. Chem. A* **2014**, *2*, 12194; e) J. Tang, Y. Yamauchi, *Nat. Chem.* **2016**, *8*, 638; f) R. R. Salunkhe, Y. V. Kaneti, J. Kim, J. H. Kim, Y. Yamauchi, *Acc. Chem. Res.* **2016**, *49*, 2796; g) R. R. Salunkhe, J. Tang, N. Kobayashi, J. Kim, Y. Ide, S. Tominaka, J. H. Kim, Y. Yamauchi, *Chem. Sci.* **2016**, *7*, 5704.
- [4] Z. Zhang, Y. Chen, X. Xu, J. Zhang, G. Xiang, W. He, X. Wang, *Angew. Chem., Int. Ed.* **2014**, *53*, 429.
- [5] a) J. Chen, X. Wang, J. Wang, P. S. Lee, *Adv. Energy Mater.* **2015**, *6*, 1501745; b) G. Fan, D. G. Evans, X. Duan, *Chem. Soc. Rev.* **2014**,

- 43, 7040; c) K. Yan, G. Wu, W. Jin, *Energy Technol.* **2016**, *4*, 354; d) Q. Wang, D. O'Hare, *Chem. Rev.* **2012**, *112*, 4124.
- [6] a) H. Hu, B. Guan, B. Xia, X. W. Lou, *J. Am. Chem. Soc.* **2015**, *137*, 5590; b) C. Sun, J. Yang, X. Rui, W. Zhang, Q. Yan, P. Chen, F. Huo, W. Huang, X. Dong, *J. Mater. Chem. A* **2015**, *3*, 8483.
- [7] a) T. Li, G. Li, L. Li, L. Liu, Y. Xu, H. Ding, T. Zhang, *ACS Appl. Mater. Interfaces* **2016**, *8*, 2562; b) G. Nagaraju, G. S. R. Raju, Y. H. Ko, J. S. Yu, *Nanoscale* **2016**, *8*, 812.
- [8] a) X. Long, Z. Wang, S. Xiao, Y. An, S. Yang, *Mater. Today* **2016**, *19*, 213; b) Z. Liu, R. Ma, M. Osada, N. Iyi, Y. Ebina, K. Takada, T. Sasaki, *J. Am. Chem. Soc.* **2006**, *128*, 4872.
- [9] a) L. Fei, B. P. Williams, S. H. Yoo, J. M. Carlin, Y. L. Joo, *Chem. Commun.* **2016**, *52*, 1501; b) R. Ramachandran, M. Saranya, C. Santhosh, V. Velmurugan, B. P. Raghupathy, S. K. Jeong, A. N. Grace, *RSC Adv.* **2014**, *4*, 21151; c) J. Mujtaba, H. Sun, G. Huang, Y. Zhao, H. Arandiyan, G. Sun, S. Xu, J. Zhu, *RSC Adv.* **2016**, *6*, 31775.
- [10] a) J. Liu, C. Wu, D. Xiao, P. Kopold, L. Gu, P. A. van Aken, J. Maier, Y. Yu, *Small* **2016**, *12*, 2354; b) H. Zhu, J. Zhang, R. Yanzhang, M. Du, Q. Wang, G. Gao, J. Wu, G. Wu, M. Zhang, B. Liu, *Adv. Mater.* **2015**, *27*, 4752.
- [11] a) Z. Yang, Z. Yao, G. Li, G. Fang, H. Nie, Z. Liu, X. Zhou, X. a. Chen, S. Huang, *ACS Nano* **2011**, *6*, 205; b) M. Wu, J. Wang, Z. Wu, H. L. Xin, D. Wang, *J. Mater. Chem. A* **2015**, *3*, 7727; c) J. Liang, Y. Jiao, M. Jaroniec, S. Z. Qiao, *Angew. Chem., Int. Ed.* **2012**, *51*, 11496; d) Y. Chang, F. Hong, C. He, Q. Zhang, J. Liu, *Adv. Mater.* **2013**, *25*, 4794.
- [12] J. Pu, Z. Wang, K. Wu, N. Yu, E. Sheng, *Phys. Chem. Chem. Phys.* **2014**, *16*, 785.
- [13] H. Chen, L. Hu, M. Chen, Y. Yan, L. Wu, *Adv. Funct. Mater.* **2014**, *24*, 934.
- [14] a) R. Xu, H. C. Zeng, *Chem. Mater.* **2003**, *15*, 2040; b) J. T. Klopogge, D. Wharton, L. Hickey, R. L. Frost, *Am. Mineral.* **2002**, *87*, 623.
- [15] a) B. M. Hunter, W. Hieringer, J. Winkler, H. Gray, A. Müller, *Energy Environ. Sci.* **2016**, *9*, 1734; b) G. Abellán, J. A. Carrasco, E. Coronado, J. Romero, M. Varela, *J. Mater. Chem. C* **2014**, *2*, 3723.
- [16] a) V. R. Constantino, T. J. Pinnavaia, *J. Inorg. Chem.* **1995**, *34*, 883; b) F. R. Costa, A. Leuteritz, U. Wagenknecht, D. Jehnichen, L. Haeussler, G. Heinrich, *Appl. Clay Sci.* **2008**, *38*, 153; c) L. Wang, Z. H. Dong, Z. G. Wang, F. X. Zhang, J. Jin, *Adv. Funct. Mater.* **2013**, *23*, 2758.
- [17] A. I. Khan, D. O'Hare, *J. Mater. Chem.* **2002**, *12*, 3191.
- [18] a) J. Yang, C. Yu, X. Fan, S. Liang, S. Li, H. Huang, Z. Ling, C. Hao, J. Qiu, *Energy Environ. Sci.* **2016**, *9*, 1299; b) J. Pu, Y. Tong, S. Wang, E. Sheng, Z. Wang, *J. Power Sources* **2014**, *250*, 250.
- [19] a) W. Zhu, X. Yue, W. Zhang, S. Yu, Y. Zhang, J. Wang, J. Wang, *Chem. Commun.* **2016**, *52*, 1486; b) K. Zeng, D. Zhang, *Prog. Energy Combust. Sci.* **2010**, *36*, 307; c) A. Sivanantham, P. Ganesan, S. Shanmugam, *Adv. Funct. Mater.* **2016**, *26*, 4661.
- [20] a) Z. F. Huang, J. Song, K. Li, M. Tahir, Y.-T. Wang, L. Pan, L. Wang, X. Zhang, J. J. Zou, *J. Am. Chem. Soc.* **2016**, *138*, 1359; b) J. Staszak-Jirkovský, C. D. Malliakas, P. P. Lopes, N. Danilovic, S. S. Kota, K.-C. Chang, B. Genorio, D. Strmcnik, V. R. Stamenkovic, M. G. Kanatzidis, *Nat. Mater.* **2016**, *15*, 197.
- [21] a) C. C. McCrory, S. Jung, J. C. Peters, T. F. Jaramillo, *J. Am. Chem. Soc.* **2013**, *135*, 16977; b) J. Tian, Q. Liu, N. Cheng, A. M. Asiri, X. Sun, *Angew. Chem., Int. Ed.* **2014**, *53*, 9577.